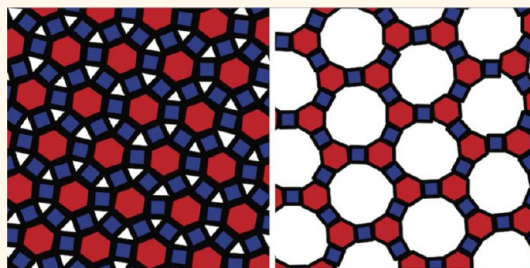


# Self-Assembly of Archimedean Tilings with Enthalpically and Entropically Patchy Polygons

Jaime A. Millan,<sup>†,§</sup> Daniel Ortiz,<sup>†,§</sup> Greg van Anders,<sup>‡</sup> and Sharon C. Glotzer<sup>†,‡,\*</sup>

<sup>†</sup>Department of Materials Science and Engineering and <sup>‡</sup>Department of Chemical Engineering, University of Michigan, Ann Arbor, Michigan 48109, United States. <sup>§</sup>J. A. Millan and D. Ortiz contributed equally to this work.

**ABSTRACT** Considerable progress in the synthesis of anisotropic patchy nanoplates (nanoplatelets) promises a rich variety of highly ordered two-dimensional superlattices. Recent experiments of superlattices assembled from nanoplates confirm the accessibility of exotic phases and motivate the need for a better understanding of the underlying self-assembly mechanisms. Here, we present experimentally accessible, rational design rules for the self-assembly of the Archimedean tilings from polygonal nanoplates. The Archimedean tilings represent a model set of target patterns that (i) contain both simple and complex patterns, (ii) are comprised of simple regular shapes, and (iii) contain patterns with potentially interesting materials properties. *Via* Monte Carlo simulations, we propose a set of design rules with general applicability to one- and two-component systems of polygons. These design rules, specified by increasing levels of patchiness, correspond to a reduced set of anisotropy dimensions for robust self-assembly of the Archimedean tilings. We show for which tilings entropic patches alone are sufficient for assembly and when short-range enthalpic interactions are required. For the latter, we show how patchy these interactions should be for optimal yield. This study provides a minimal set of guidelines for the design of anisotropic patchy particles that can self-assemble all 11 Archimedean tilings.



**KEYWORDS:** self-assembly · patchy particles · Monte Carlo simulation · nanoplates · predictive design · entropic forces

Tessellations composed of regular polygons that completely tile the two-dimensional Euclidean plane have been studied since ancient times due to their mathematics and visually attractive symmetries.<sup>1</sup> Johannes Kepler identified 11 plane-filling tilings known as the Archimedean tilings (ATs),<sup>2</sup> which can be divided into two groups, namely, regular (Figure 1a,d,g) and semiregular tilings (Figure 1j–q) made from regular polygons. The regular tilings are characterized by the ability to map flags (tuples of mutually incident vertices, edges, and tiles) *via* tiling-related group symmetry actions (flag-transitivity), while the remaining semiregular tilings are expanded with a more relaxed symmetry in mapping vertex pairs to each other by an acting group symmetry pertaining to the tiling (vertex-transitivity).<sup>1</sup>

Various materials on multiple length scales are known to form the ATs, which exhibit striking photonic<sup>3</sup> and diffusive

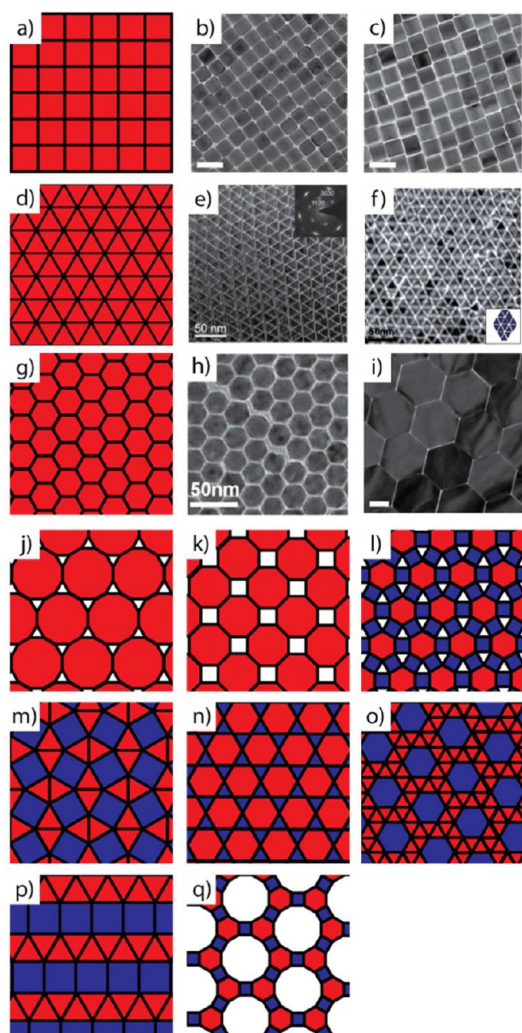
properties.<sup>4</sup> The (4.6.12) and (3<sup>2</sup>.4.3.4) ATs possess complete photonic band gaps.<sup>3</sup> Regular and semiregular tilings are commonly observed in bulk solids, polymeric assemblies, and nanomaterials. Archimedean crystalline nets such as in Al<sub>2</sub>O<sub>3</sub> (6<sup>3</sup>) and CuAl<sub>2</sub> (3<sup>2</sup>.4.3.4) describe the coordination polyhedra in various crystals of complex alloys.<sup>5</sup> The more complex semiregular tilings have been observed in the bulk structure of metallic alloys<sup>6</sup> and supramolecular interfacial tessellations.<sup>7,8</sup> Manifestations of regular and semiregular tilings have been observed in liquid crystal<sup>9</sup> (T-shaped molecules) and polymer systems<sup>10</sup> (ABC star branched polymers) and in systems of patchy nanocrystals.<sup>11</sup> The self-assembly of a decagonal quasicrystalline substrate has been shown to self-assemble the (3<sup>3</sup>.4<sup>2</sup>) and (3<sup>6</sup>) ATs.<sup>12</sup> Patchy triblock Janus colloids self-assemble the (3.6.3.6) AT.<sup>13</sup> Most of those results represent the ATs in a vertex-to-vertex representation where particle

\* Address correspondence to sglotzer@umich.edu.

Received for review January 9, 2014 and accepted February 2, 2014.

Published online February 02, 2014 10.1021/nn500147u

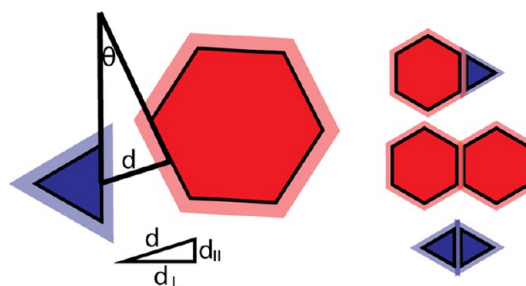
© 2014 American Chemical Society



**Figure 1.** The 11 space-filling Archimedean tilings and published images of representative assemblies of the triangular ( $3^6$ ), square ( $4^4$ ), and hexagonal ( $6^3$ ) AT tilings. Regular tilings: (a) square ( $4^4$ ), (d) triangular ( $3^6$ ), and (g) hexagonal ( $6^3$ ). The experimental images of the regular tilings are (b) ( $4^4$ )  $\beta$ - $\text{NaYF}_4$  AT,<sup>27</sup> (c)  $\text{NaYF}_4$ : Yb/Er ( $4^4$ ) AT,<sup>27</sup> (e)  $\text{LaF}_3$  ( $3^6$ ) AT,<sup>32</sup> (f)  $\text{Cu}_{2-x}\text{Se}$  ( $3^6$ ) AT,<sup>28</sup> (h)  $\text{Cu}_{2-x}\text{Se}$  ( $6^3$ ) AT,<sup>28</sup> and (i)  $\beta$ - $\text{NaYF}_4$  ( $6^3$ ) AT.<sup>27</sup> Semiregular tilings: (j) truncated hexagonal ( $3.12^2$ ), (k) truncated square ( $4.8^2$ ), (l) rhombitrihexagonal ( $3.4.6.4$ ), (m) snub square ( $3^2.4.3.4$ ), (n) trihexagonal (or kagome) ( $3.6.3.6$ ), (o) snub hexagonal ( $3^4.6$ ), (p) elongated triangular ( $3^3.4^2$ ), and (q) truncated trihexagonal ( $4.6.12$ ) tilings, which comprise the entire family of Archimedean tilings. In our simulations we consider colored and white polygons as hard nanoplatelets and pores, respectively.

centers are placed at the vertices of the polygons in the tiling. The diversity of nanoscopic and microscopic components that assemble ATs motivates a need to understand the minimal design rules needed for the assembly of these tilings, in particular from readily accessible 2D nanoplates.

Anisotropic 2D nanoplates are known to have interesting electronic,<sup>14</sup> catalytic,<sup>15</sup> and optical<sup>16</sup> properties and have been shown to successfully form exotic superlattices *via* a subtle balance between shape-induced entropic patchiness<sup>17</sup> and ligand-induced



**Figure 2.** Schematic indicating the shape-specific interactions between nanoplates used for the shape-selective interaction case. (Left) Each shape is surrounded by a soft shell, which represents the range of the enthalpically patchy interaction. The interaction between the nanoplates is edge-to-edge and short-ranged and depends on the distance shift  $d_{||}$ , the normal distance  $d_{\perp}$ , and angle ( $\theta$ ) between the edges. (Right) Schematic for hexagon–hexagon, hexagon–triangle, and triangle–triangle interaction, showing the selectivity of the patchy interaction.

enthalpic patchiness.<sup>18,19</sup> 2D assemblies of nanoplates could be used in thin film electronics.<sup>20</sup> Also, 2D assemblies of perovskite nanoparticles, such as  $\text{PbTiO}_3$  nanoplates,<sup>21</sup> have interesting ferroelectric and storage properties.<sup>22</sup> Given their polygonal shape, faceted nanoplates could potentially self-assemble the ATs. Although assemblies of ATs from polygonal nanoplates have been reported in experiments,<sup>23–33</sup> they are restricted to the regular ATs (those composed of a single type of tile) (Figure 2). Because faceted nanoplates can exploit both entropic and enthalpic patchy interactions, they represent a viable approach that could reduce the complexity of the design rules for self-assembly of elusive irregular and porous tilings, when compared to the vertex-to-vertex approach.

Numerical simulations have also predicted the self-assembly of the Archimedean tilings. For spherical particles, simulations of patchy particles<sup>34,35</sup> reported the self-assembly of all ATs except for the ( $3.6.3.6$ ) AT. Ditettered nanospheres<sup>36</sup> formed the ( $4.8^2$ ) and ( $6^3$ ) ATs. Lock and key colloids<sup>37</sup> and hard polyhedra<sup>38,39</sup> formed the ( $3^2.4.3.4$ ) and ( $6^3$ ) ATs, respectively. Despite these studies, numerical simulations have neglected the commonly synthesized polygonal nanoplates as a means of AT self-assembly.

Here, we report the minimal set of interactions needed to self-assemble experimentally accessible ATs from regular polygons, mimicking nanoplates assembled into crystalline monolayers (Figure 1). We show through Monte Carlo simulations the self-assembly of these tilings by exploiting entropic and enthalpic interactions encoded in the shape of the polygons. We arrive at a design strategy for patchy polygon particles that is accessible to current experimental techniques and present the minimal set of design rules for each AT. We report that four ATs, namely, the ( $6^3$ ), ( $3^6$ ), ( $4^4$ ), and ( $3.12^2$ ) tilings, can be assembled solely with hard interactions, highlighting the role of directional entropic forces<sup>39,40</sup> that arise from the particle shape.

We quantify the strength of these entropic patches<sup>17</sup> by calculating the potential of mean force and torque using free energy calculations.<sup>40</sup> Symmetric enthalpic patches ((4.8<sup>2</sup>)), shape-specific patches ((3<sup>2</sup>.4.3.4), (3.4.6.4), (3.6.3.6)), and edge-specific patches ((3<sup>3</sup>.4<sup>2</sup>), (3<sup>4</sup>.6), (4.6.12)) are needed to self-assemble the remaining crystalline structures. Beyond the ATs, the design rules presented provide general insight into the design of complex crystal structures using anisotropic building blocks.

## MODEL AND APPROACH

Each nanoplate is modeled as a hard convex regular polygon with a finite number of edges,  $N = 3, 4, 6, 8,$  and  $12$ . In the first model—that of least complexity—no additional interactions are included. Initially, we find those ATs ((3<sup>3</sup>), (4<sup>4</sup>), (6<sup>3</sup>), (3.12<sup>2</sup>)) that can be assembled by entropic forces alone. In all cases, shape anisotropy gives rise to entropic patchiness that emerges upon crowding and is density dependent.<sup>40</sup>

For the remaining ATs, we introduce a short-range attractive edge-to-edge interaction potential. The interaction potential is divided into parallel, perpendicular, and angular components (Figure 2). The parallel component represents the amount of parallel contact between interacting edges. The perpendicular component models the commonly observed attractive van der Waals force between ligand-capped nanocrystals,<sup>41–43</sup> depends on the distance between centers of edges, and is approximated by a parabolic well. The angular component penalizes any misalignment between neighboring nanoplates representing steric forces between ligand shells. A halo drawn around the building block represents the interaction range of the edge–edge pair potential (Figure 2). Different colors represent different interaction strengths between edges. These enthalpic patches act as reversible, directional, “sticky” bonds that compete or combine with entropic patches. The justification of such a short-range potential in a nanoplate system is based on the presence of adsorbed ligands (e.g., oleic acid molecules).<sup>18,44</sup>

The complexity of the edge-to-edge interactions is determined by the targeted AT. We use three enthalpic models of increasing complexity for the assembly of the remaining ATs: symmetric, shape-specific, and edge-specific. The first enthalpic model treats the pairwise interaction between polygons as patches of equal strength distributed over all edges. The second enthalpic model (“shape-specific”), which is a modification of the previous model, tunes the interaction strength between patches of dissimilar polygons for those ATs composed of binary tile mixtures. The third enthalpic model (“edge-specific”) further increases the interaction complexity and determines the interaction strength based on the type of edges even for similarly shaped particles. To quantify the interaction

asymmetry between different edges, we introduce the parameter  $\sigma$ . The  $\sigma$  values reported are the minimum asymmetry needed to assemble the target ATs. For each AT tiling, we find a favorable thermodynamic state point for self-assembly of the building block.

## RESULTS

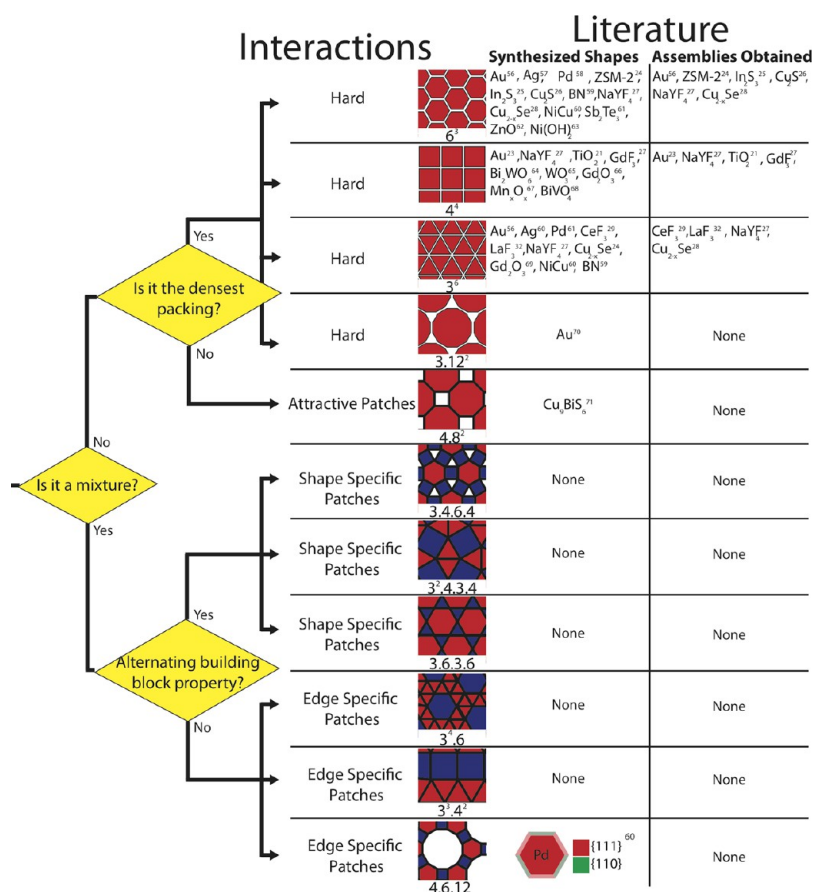
We present our findings in four categories based on the four types of interaction sets needed to assemble the Archimedean tilings: (i) entropic, (ii) symmetric, (iii) shape-specific, and (iv) edge-specific enthalpic interactions. All ATs can be self-assembled with these four interaction approaches. The results are summarized in Figures 3 and 8.

**i. Entropic Interactions.** Directional entropic forces arising from shape entropy, or a drive to local dense packing, are an entropic strategy to self-assemble the Archimedean tilings.<sup>17,37,42–46</sup> In our studies, by changing the number of vertices of the building block, regular polygons are shown to self-assemble four of the ATs.

Regular triangles and squares form the (3<sup>6</sup>) and (4<sup>4</sup>) ATs, respectively (Figure S1a,b). Insets show the regular polygon building block and a close-up of the assembly. The accompanying diffraction patterns show sharp peaks in hexagonal and square reciprocal lattices for triangles and squares, respectively, as a manifestation of long-range order. The small number of defects highlights the robustness of the assembly of both regular triangular and square tilings. However, there exists a collection of crystalline structures that differ from the triangle and square ATs solely by a shift vector along the lattice axes. Although at infinite pressure all of these tilings belong to a thermodynamically stable degenerate set with equal probability for self-assembly, we observe that at finite pressures the (3<sup>6</sup>) and (4<sup>4</sup>) ATs are the equilibrium configurations. Previous work has also shown that the equilibrium structures of hard triangles and squares at high packing fractions are the (3<sup>6</sup>) and (4<sup>4</sup>) ATs, respectively.<sup>47–49</sup> Hard hexagons readily form the (6<sup>3</sup>) AT (Figure S1c) at finite pressures. This is the unique infinite pressure (maximum density) crystal structure for the regular hexagon due to shape constraints.

All of the ATs are, by definition, space filling. However, by treating some tile types as pores, it is possible to assemble some multitile ATs with a single nanoplate shape. An example of this is the (3.12<sup>2</sup>) AT, which is composed of dodecagons and triangles. We find that regular dodecagons easily self-assemble into the truncated hexagonal Archimedean tiling at finite pressures without explicit triangle tiles, that is, treating the triangles as pores in the tiling (Figure S1d). Notably, this assembly is also the infinite pressure crystal for hard dodecagons.<sup>50</sup>

To summarize the results thus far, for each of the four (regular) ATs just discussed, entropy alone is



**Figure 3.** Flow diagram representing the design process for the ATs. The paths show how to self-assemble the ATs. Hard interactions are for assemblies that coincide with their densest packings in single-component systems. Shape-specific patches are for mixtures with lines of alternating building blocks. Mixtures with complex bond networks need edge-specific patches. The two rightmost columns show the state-of-the-art in particle synthesis and self-assembly for each corresponding AT.

sufficient to obtain the tiling *via* thermodynamic self-assembly. This can be understood as follows. The triangular and square lattice tilings require that its constituents be edge-to-edge. From an entropic standpoint, there are an infinite number of tilings by arbitrarily translating rows or columns of triangles and squares. The self-assembly of edge–edge ATs at finite density implies that there is a free energy difference between aligned and misaligned states. Free energy calculations were performed to quantify the effect of alignment on the free energy. The effects of density and shape were explored (Figure 4a,b). For dense fluids of hard triangles (Figure 4a,b), there is a free energy difference between the aligned and misaligned state of  $1.2k_B T$ . Above and near the crystallization packing fraction ( $\rho = 0.75$ ) the free energy difference increases to  $2.5k_B T$ . The increase in free energy at high packing fraction penalizes misalignments and drives the system to the (3<sup>6</sup>) AT. On the other hand, the degree of faceting has an inverse effect on the free energy. As the number of facets increases, a polygon behaves more like a disk. Indeed we observe that the directional entropic forces lose directionality for increased faceting. Directional entropic forces weaken considerably

with the number of facets since they arise from a drive toward dense local packing, and the local packing becomes less dense as the number of facets increases.<sup>17</sup> For example, the hard triangle has an entropic penalty of  $2.5k_B T$  for misalignment, whereas at the same density the dodecagon has an entropic penalty of only  $0.3k_B T$ . For the ATs with degenerate ground states, such as the (3<sup>6</sup>) and (4<sup>4</sup>) ATs, directional entropic forces explain the preferential edge–edge alignment of the assemblies. They also explain the thermodynamic stability of the (3.12<sup>3</sup>) and (6<sup>3</sup>) Archimedean tiling at finite packing fractions. As a final note, we observed that the inclusion of attractive patchy interactions does not inhibit the formation of any of these four ATs.

**ii. Symmetric Enthalpic Interactions.** We find that entropy alone is insufficient to assemble the remaining ATs, and enthalpic interactions must be included. In these cases, enthalpy biases the free energy to promote edge–edge binding and can stabilize open structures that would not be possible with purely entropic forces.

Like the (3.12<sup>3</sup>) AT, the (4.8<sup>2</sup>) AT can be most easily assembled using only octagons and treating the square tiles as pores. However, because hard octagons

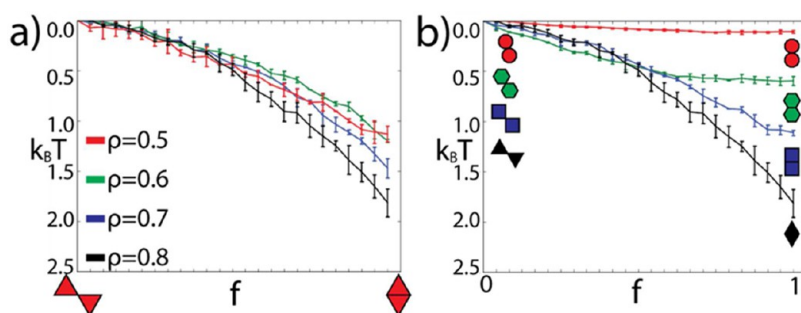


Figure 4. (a) Effective free energy difference between different configurations of hard triangles as a function of density. (b) Effect of shape on the effective free energy difference at fixed density. The free energy difference is shown as a function of misalignment factor  $f$ , which quantifies the edge–edge coverage between two pairs of anisotropic particles. In (a), the free energy gain for edge–edge alignment in triangles is  $1.2k_B T$ ,  $1.2k_B T$ ,  $1.5k_B T$ , and  $1.8k_B T$  at density fractions 0.5, 0.6, 0.7, and 0.8, respectively. In (b), the free energy gain for edge–edge alignment at packing fraction 0.8 is  $2.5k_B T$  for triangles,  $1.1k_B T$  for square,  $0.6k_B T$  for hexagons, and  $0.2k_B T$  for dodecagons (b).

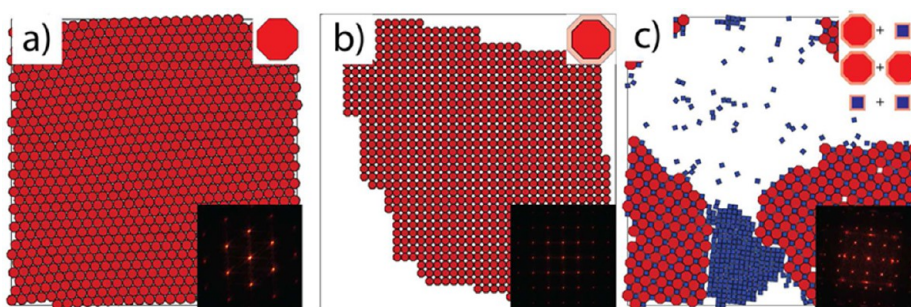


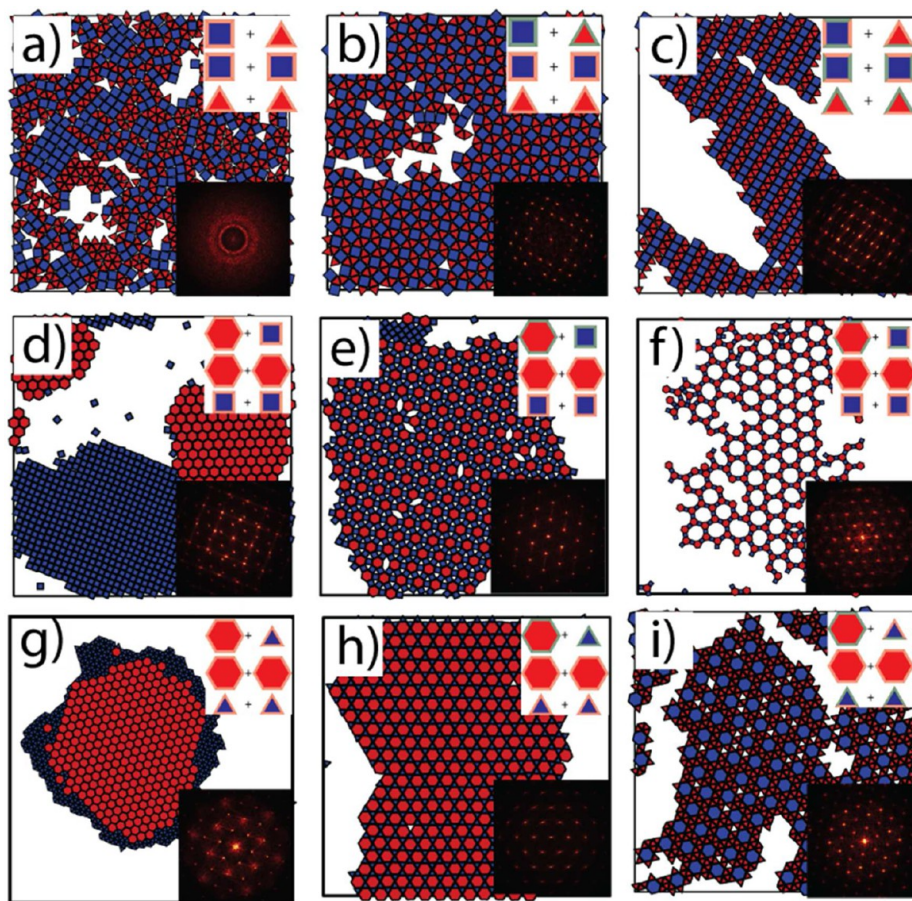
Figure 5. Hard vs symmetrically attractive octagons. (a) Hard octagons (upper-left inset) assemble into a hexagonal crystal structure. (b) Symmetric attractive octagons (upper-right inset) form the defect-free  $(4.8^2)$  AT where the squares are treated as pores. Both snapshots are accompanied by a diffraction pattern showing long-range order. (c) Truncated square tiling formed from octagons and squares with symmetric attractive interactions in a 1:2 mixture ratio. Excess squares formed the  $(4^4)$  square tiling upon further annealing.

favor a hexagonal crystal structure (Figure 5a), attraction between nanoplate edges is required to stabilize the AT. The hexagonal crystal structure has misaligned edge–edge bonds with an entropic penalty of  $\sim 0.5k_B T$  per edge at  $\rho \geq 0.8$ . The two barriers to entropic self-assembly of the  $(4.8^2)$  AT with hard octagons are packing constraints and the coordination of this semiregular tiling. At  $\rho \geq 0.8284$ , the  $(4.8^2)$  AT cannot self-assemble due to particle overlaps. At lower packing fractions, the free energy penalty for misalignment is  $\sim 0.2k_B T$ . Two-thirds of the edge–edge octagons are 50% misaligned, while the remaining bonds are aligned in the hexagonal crystal structure. The hexagonal crystal structure exhibits a higher coordination (six nearest neighbor bonds) as compared to the truncated square AT (four nearest neighbor bonds), which compensates for the entropic penalty due to misalignments. The partial misalignments of the hexagonal crystal structure are entropically favored to the aligned edge–edge bonds of the  $(4.8^2)$  Archimedean tiling due to the effect of coordination and packing constraints. In simple terms, the ideal  $(4.8^2)$  Archimedean crystalline structure with regular octagons has a packing fraction of 0.8284. This value is below the maximum packing fraction of hard regular octagons, which tend to form the hexagonal structure.

Consequently, we anticipate attractive interactions are needed to stabilize the  $(4.8^2)$  AT. Indeed, by adding short-ranged attractive patches of strength  $\varepsilon$  to each edge of the octagon, we find the  $(4.8^2)$  AT robustly self-assembles (Figure 5b). Binary mixtures of octagons and squares with attractive patches also form this semiregular AT (Figure 5c). It is interesting to note that the AT forms without the perfect stoichiometric ratio of tiles. The excess squares form the  $(4^4)$  AT. This result is important because experiments will not be constrained by stoichiometry in seeking the  $(4.8^2)$  AT (Figure 5c).

**iii. Shape-Specific Enthalpic Interactions.** The five ATs studied thus far were each assembled using a single tile shape, even when multiple tiles technically compose the tiling and one of the tile shapes is considered a pore. The remaining six ATs all require a minimum of two tile shapes. Of these, three— $(3^2.4.3.4)$ ,  $(3.4.6.4)$ , and  $(3.6.3.6)$ —require shape-specific interactions (Figure 6b,e,h, respectively). As defined previously, shape specificity implies that the interaction between *dissimilar*—rather than *similar*—species is favored, an asymmetry recently observed in rod–sphere shape alloys.<sup>44</sup>

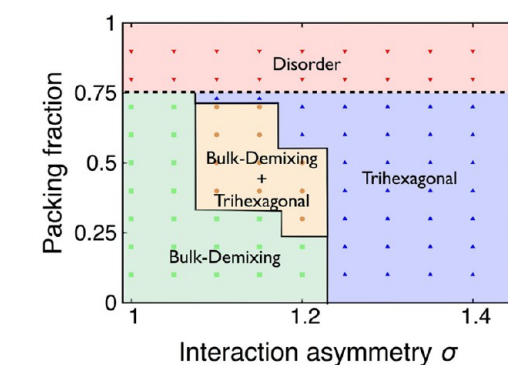
The two insets of each panel in Figure 6 highlight the matching rules between polygons and the corresponding diffraction pattern of the assembly.



**Figure 6.** Representative snapshots of the design process for the  $(3^2.4.3.4)$ ,  $(3.4.6.4)$ ,  $(3.6.3.6)$ ,  $(3^3.4^2)$ ,  $(3^4.6)$ , and  $(4.6.12)$  ATs. Insets show the design rules and a diffraction pattern. A red halo implies a weakly attractive interaction, while a green halo implies a strong attractive interaction. Left column panels show symmetrically attractive mixtures of (a) square–triangle, (d) square–hexagon, and (g) triangle–hexagon mixtures. Center column panels correspond to the mixtures in the left column with shape-specific patches that readily self-assemble (b) the  $(3^2.4.3.4)$ , (e)  $(3.4.6.4)$ , and (h)  $(3.6.3.6)$  ATs. Right column panels show shape-specific attractive square–triangle, hexagon–square, and hexagon–triangle mixtures that self-assemble the (c)  $(3^3.4^2)$ , (f)  $(4.6.12)$ , and (i)  $(3^4.6)$  ATs, respectively.

The matching rules show all combinations of building blocks and the strength of each edge–edge interaction for all interaction pairs. The interaction strength ( $\epsilon$ ) is visualized by the color of the halo around the building block, where red is weak and green is strong. The strength of the strong interaction depends on the targeted AT, as discussed below.

Binary mixtures of symmetric attractive polygons demix or form disordered aggregates (Figure 6a, d and g). Square–triangle mixtures with symmetric interactions tend to be disordered at intermediate densities because the difference in the free energies of the demixed (pure square and pure triangle) phase vs the mixed phase is small (Figure 6a). In contrast, hexagon–square and hexagon–triangle mixtures with symmetric interactions demix at intermediate densities (Figures 6d,g and 7). Symmetrically attractive mixtures of regular hexagons and triangles using the stoichiometry of the  $(3.6.3.6)$  AT demix and form, as coexisting phases, the  $3^6$  and  $6^3$  ATs (Figure 6g). Similarly, symmetrically attractive mixtures of the rhombitrihexagonal  $(3.4.6.4)$  AT demix into pure hexagonal and square ATs



**Figure 7.** Phase diagram of packing fraction vs interaction asymmetry  $\sigma$  for hexagon–triangle mixtures. Symbols represent simulation data points for different asymmetry interaction (shape-specific attraction) and packing fraction values. Each data point represents either the predominantly or always observed phase upon slow annealing ( $10^7$  time steps) in multiple parallel (five or more) simulations for a given density and interaction asymmetry with systems of 1000 particles.

(Figure 6d). This natural trend to demixing is also observed in mixtures of hard polygons of the same

shapes. In the presence of symmetric attractions, we observe a hierarchy of freezing temperatures. Below but close to the first freezing temperature, the polygons with the most edges crystallize first since these polygons possess more enthalpic bonds (higher crystal coordination), while the less faceted polygons remain in a liquid phase. Further cooling to the second freezing temperature leads to the crystallization of the smaller polygons. As the difference in the number of enthalpic edges of both particles increases, so does the separation between these two freezing temperatures. Thus for square–triangle mixtures the difference is small, leading to disorder. For hexagon–triangle and hexagon–square mixtures the difference between melting temperatures increases ( $(T_1 - T_2)/T_1 \approx 0.2$ , where  $T_1$  and  $T_2$  are the first and second freezing temperatures), leading to complete bulk demixing.

By biasing the opposite shape interaction (hexagon–triangle, square–triangle, hexagon–square) using shape-specific interactions, the  $(3^2.4.3.4)$ ,  $(3.6.3.6)$ , and  $(3.4.6.4)$  ATs will self-assemble (Figure 6b,e,h). The  $(3.4.6.4)$  tiling was self-assembled as a binary mixture because the ternary mixture matching rules are more complex. Thus, a pore acts as the triangle tile in this patchy polygon design. The minimum asymmetry  $\sigma$  in the interaction strength to self-assemble the  $(3^2.4.3.4)$ ,  $(3.6.3.6)$ , and  $(3.4.6.4)$  ATs is  $1.3\varepsilon$ ,  $1.3\varepsilon$ , and  $1.5\varepsilon$ , respectively.

Changing  $\sigma$  affects the phase behavior, as shown in Figure 7, where we present the phase diagram of hexagon–triangle systems based on  $\sigma$  and density. This mixture shows rich phase behavior characterized by the formation of a (bulk) demixed phase, the targeted trihexagonal AT, and a coexistence region between these two phases. As previously discussed, symmetric mixtures ( $\sigma = 1\varepsilon$ ) demix fully. Small perturbations from symmetric mixtures yield the same results. However, for a particular range of interaction asymmetry ( $1.1\varepsilon < \sigma < 1.25\varepsilon$ ), coexistence between the targeted trihexagonal AT and the completely demixed phase appears for certain densities, indicating the possibility that the trihexagonal AT could be observed at slightly higher densities. Indeed, we observe the trihexagonal AT at packing fractions of  $\sim 0.725$ . The coexistence region is characterized by three successive melting stages upon slow cooling. At high temperature, shapes with more edges (hexagons) crystallize, while shapes with lower edges (triangles) form a wetting liquid. Further annealing to lower  $T$  leads to the formation of the ATs because they are the ground state at low temperature. Finally, excess triangles excluded from the AT crystallize into the  $3^6$  AT. Further increase in interaction asymmetry ( $\sigma \geq 1.25\varepsilon$ ) stabilizes the targeted AT at low and high density, implying that shape-specific interactions can overcome the trend toward demixing at intermediate and lower densities (Figure 7). At packing fractions of  $\geq 0.8$ , disordered


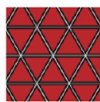

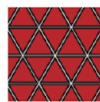
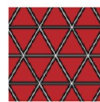

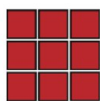
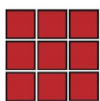
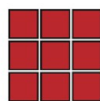
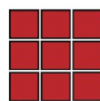

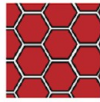
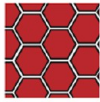
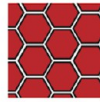
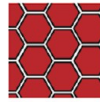

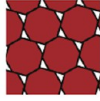
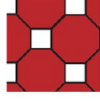

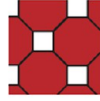









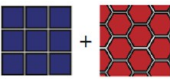

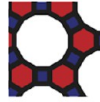

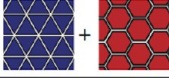


arrangements are formed regardless of interaction asymmetry. Hexagon–square and square–triangle mixtures exhibit a similar rich phase behavior, with the exception that square–triangle mixtures form a single disordered phase instead of (bulk) demixed phases (Figures 6a and 8).

**iv. Edge-Specific Enthalpic Interactions.** In the previous section, shape-specific interactions of triangle–square, hexagon–square, and hexagon–triangle shape alloys were shown to self-assemble the  $(3^2.4.3.4)$ ,  $(3.4.6.4)$ , and  $(3.6.3.6)$  ATs. The mixtures that self-assemble the  $(3^2.4.3.4)$ ,  $(3.4.6.4)$ , and  $(3.6.3.6)$  ATs have a similar mixing ratio as the  $(3^3.4^2)$ ,  $(3^4.6)$ , and  $(4.6.12)$  ATs. The mixing ratio for the  $(3^4.6)$  AT (triangle-to-hexagon 8:1) is greater than that of the  $(3.6.3.6)$  tiling. For a triangle-to-hexagon 8:1 mixture ratio, we observe coexistence between the  $(3.6.3.6)$  tiling and a triangular tiling formed by excess triangles (Figure 8). The demixing observed between excess triangles and the self-assembled  $(3.6.3.6)$  AT is similar to that observed between excess squares and the  $(4.8^2)$  AT. As shown before, shape-specific interactions for these mixtures self-assemble the  $(3^2.4.3.4)$ ,  $(3.4.6.4)$ , and  $(3.6.3.6)$  ATs (Figure 6b,e,h).

Edge-specific patchy interactions increase the interaction specificity. As previously mentioned (Model and Approach section), edge-specific interactions are a type of interaction in which each edge pair can have unique interaction strength  $\varepsilon_{ij}$ , where  $i$  and  $j$  correspond to edge indices on different building blocks. Edge-specific interactions allow the self-assembly of complex crystalline structures and occur naturally in crystalline nanoplates due to energetic differences between different crystallographic edges.<sup>18</sup>

The minimal designs of the  $(3^3.4^2)$ ,  $(4.6.12)$ , and  $(3^4.6)$  AT are shown in Figure 6 c, f and i. In the case of the elongated triangular AT, self-assembly requires strong attraction between opposite edges of the square and one edge of the triangle and a stronger attraction between the edges that do not attract triangles. The edge pair of the triangles that do not attach preferentially to squares interact strongly. The assembly in Figure 6c requires a strong interaction asymmetry of  $\sigma = 1.2\varepsilon$  (green edges). The design biases energetically the unit cells of the  $(3^3)$  AT. The minimal design for the  $(4.6.12)$  Archimedean tiling requires strong attraction ( $\sigma = 1.25\varepsilon$ ) between alternating edges of hexagon and squares. The remaining edges of both shapes are weakly attractive (inset in Figure 6f). Hexagons and squares form rings, which is consistent with the truncated hexagonal AT. The assembly is not free of defects, and in some cases single or multiple polygons are encircled by these rings (Figure 6f).

In the minimal design for the  $(3^4.6)$  Archimedean tiling, all edges of the hexagon preferentially attach to one specific edge on the triangles, the hexagon-to-hexagon edge attraction is weak ( $\sigma = 1\varepsilon$ ), and triangles

	Hard	Attraction	Shape Specific Patches	Edge Specific Patches
				
				
				
				
				
	Disordered	Disordered		
	Disordered	Demixing 		
	Disordered	Demixing 		

**Figure 8. Simulation results summary.** The first column shows the polygons necessary for the assembly of ATs under the design rules proposed. The remaining columns indicate the configurations observed with the different interaction sets.

preferentially attach to each other on edges that do not preferentially attract hexagon edges (Figure 6i). By making the hexagon preferentially attractive to one side of the triangle, all edges of the hexagon become saturated and the triangle–triangle interaction completes the tiling. For the assembly in Figure 6f, the interaction asymmetry  $\sigma$  is  $3\varepsilon$ . Due to the complexity of this set of design rules, multiple point defects are observed. This AT is chiral; however no bias toward either handedness was observed. Thus, to form the snub hexagonal AT with a targeted chirality, further complexity in polygon patchiness is needed.

## DISCUSSION

We approached the design of nanoplates to assemble the Archimedean tilings by ascertaining the simplest set of interactions yielding the desired tiling. The multistep design process summarized on the left-hand side in Figure 3 uses information about the target tiling and building block. We first minimize the number of building blocks to self-assemble the targeted tiling. For

the  $(3.12^2)$ ,  $(4.8^2)$ ,  $(3.4.6.4)$ , and  $(4.6.12)$  ATs, one of the polygonal tiles is replaced by a pore, and the resulting tiling no longer fills space, but is instead “open” and porous.

After selecting the building blocks, the design process examined the constituent polygonal building blocks and alters the interaction complexity by changing the specificity of interactions. The four models ranked in terms of specificity are hard, symmetric patches, shape-specific patches, and edge-specific patches. Our design process reveals why for each AT a certain degree of specificity is needed for self-assembly. Initially, we test if entropic interactions are sufficient to self-assemble each crystalline structure. If the infinite pressure ground state is not the candidate crystal structure, we find attractive interactions are needed to self-assemble the crystalline structure (Figure 3). Due to the highly symmetric polygons used to self-assemble the ATs, we argue that an effective entropic edge–edge interaction will stabilize these highly symmetric ground states. For crystal structures with one



building block that are not the infinite pressure ground state, symmetric attractive patches are sufficient for assembly (Figure 3). For mixtures of building blocks, the complexity of the crystal structure determines the complexity of the interaction potential. Hard (entropic) mixtures show a natural trend to partial demixing and do not form crystalline monolayers with discrete symmetries. Symmetric attractive mixtures also demix, with no indicative behavior toward the formation of binary ATs at intermediate densities. We posit that the hard mixtures segregate due to a depletion effect.<sup>51</sup> Since hard and symmetrically attractive building blocks demix, selective patchiness must be used to overcome this natural trend (Figure 3). The local environment for each polygonal tile in the target AT determines the arrangement of patches. If an alternating building block crystal structure is present, shape-specific patches are sufficient to design the crystalline structure (Figure 3). An alternate building block structure is a binary mixture in which the large polygonal tile is surrounded by the small tile, and the small tile has at most one bond with another small tile. If the crystalline structure for a mixture of building blocks does not contain the alternating building block property, it is necessary to use edge-specific interactions. The assembly complexity of the building block and crystal structure provides the necessary information to self-assemble the AT.

The description of minimal design rules for self-assembly is related to tiling models in computer science and mathematical descriptions of graph connectivity. The general complexity of edge connectivity problems is known to be NP hard,<sup>52</sup> which weakens the attractiveness of an algorithmic approach to the development of design rules for crystal structures. Mathematical work on the edge coloring of Archimedean graphs<sup>53</sup> does not provide sufficient information to develop design rules for self-assembly. In effect, an iterative, heuristic approach as described in this paper is the best one can do to develop design rules for self-assembly of tilings such as these.

## CONCLUSION

Ascertaining assembly complexity is an essential feature of our design strategy for mixtures of anisotropic patchy particles. We ranked each AT from (3<sup>6</sup>) to the (4.6.12) in order of assembly complexity. Self-assembly complexity is the complexity of the simplest

set of interactions and building blocks that self-assemble the candidate crystal structure with a minimal number of crystallographic defects (Figure 3). We described the design strategy in a flow diagram (Figure 3). The flow diagram describes the steps used to design the interactions of the building blocks. To the right of the design flow diagram, we overview material systems<sup>54–69</sup> that can form the anisotropic nanoplates consistent with the ATs and material systems that self-assemble<sup>23–33</sup> ATs with nanoplates (Figure 1). The entropically stabilized (3<sup>6</sup>), (4<sup>4</sup>), and (6<sup>3</sup>) ATs have been observed experimentally with polygonal tiles, but the other Archimedean tilings remain elusive (Figures 1 and 3). To assemble these elusive ATs, nanoplates can be covered with DNA.<sup>70–72</sup> DNA-functionalized tiles provide a means of achieving the necessary interaction specificity to assemble ATs. Also, we note that nanoplates with different crystallographic edges can act as effective patchy particles.<sup>18</sup> We propose that edge-specific nanoparticle patches can be synthesized by exploiting the different attractive energies of the crystallographic facets.<sup>19</sup>

The building block design process offers insight into the necessary conditions to self-assemble crystals with regular polygons (nanoplates). The design process has led to important conclusions about shape and self-assembly, summarized in Figure 8. With only entropy, certain Archimedean tilings can self-assemble their infinite pressure packings at intermediate packing fractions. This finding reinforces the perspective on an entropic “patch” as a driver for self-assembly.<sup>17</sup> On the other hand, for low-density packings symmetric enthalpic patches are required. Binary mixtures of regular shapes have a rich behavior that depends on the type of interactions and geometry. We observe that hard binary mixtures tend to be disordered when mixed. By adding enthalpic patches, demixing occurs if the difference between the coordination of the polygons is large. This is confirmed by the observed demixing of hexagon–square and hexagon–triangle assemblies, whereas square–triangle mixtures are disordered. Shape-specific and edge-specific patches stabilize the remaining semiregular tilings. Although nanoplate patterning inspires the designs developed in this work, these enthalpic design rules can also be expanded to supramolecular systems, where particle interactions are programmable and system dynamics are faster.

## METHODS

**MC Simulations.** Directional interactions were modeled by storing matching rules in a hash table. The edge–edge matching rules contain particle pair information to evaluate the interaction potential. Each edge–edge matching rule contains each particle type, two edges, and a well depth. To model a short-range interaction, the range was set to 20% of the edge

length of the polygons. Ranges between 10% and 30% gave similar results, with 20% providing optimal assembly propensity. Thus, the interaction potential is a function of the two closest edge pairs, the distance between the edges, the angle between the edges, and the particle types.

For the purely entropic case, simulations are carried out using an NPT MC algorithm. The pressure is slowly increased

over time, and overlap checks are performed using the GJK algorithm.<sup>72</sup> For the three enthalpic models, NVT simulations were performed using established Monte Carlo methods.<sup>18</sup> The number of particles was varied between 900 and 2000 to ensure the absence of finite size effects. We equilibrate each simulation by annealing each system for  $10^7$  time steps and also gathered statistics for  $\sim 10^7$  time steps.

**Conflict of Interest:** The authors declare no competing financial interest.

**Supporting Information Available:** Simulation snapshots. This material is available free of charge via the Internet at <http://pubs.acs.org>.

**Acknowledgment.** D.O and J.A.M. acknowledge M. Engel for help with algorithm development and fruitful discussions. This work was supported in part by the U.S. Army Research Office under Grant Award No. W911NF-10-1-0518 and partially supported by a Simons Investigator award from the Simons Foundation to S.C.G. J.A.M., D.O., and S.C.G. acknowledge support by the Assistant Secretary of Defense for Research and Engineering, U.S. Department of Defense, under Award No. N00244-09-1-0062. Any opinions, findings, and conclusions or recommendations expressed in this publication are those of the author(s) and do not necessarily reflect the views of the DOD/ASD(R&E).

## REFERENCES AND NOTES

- Grünbaum, B.; Shephard, G. C. *Tilings and Patterns*; W H Freeman and Co.: New York, 1987.
- Kepler, J. *Harmonices Mundi*; Johannes Planck: Linz, 1619.
- Ueda, K.; Dotera, T.; Gemma, T. Photonic Band Structure Calculations of Two-Dimensional Archimedean Tiling Patterns. *Phys. Rev. B* **2007**, *75*, 195122.
- Basnarkov, L.; Urumov, V. Diffusion on Archimedean Lattices. *Phys. Rev. E* **2006**, *73*, 046116.
- O'Keeffe, M.; Hyde, B. G. Plane Nets in Crystal Chemistry. *Philos. Trans. R. Soc. A* **1980**, *295*, 553–618.
- McMahon, M.; Degtyareva, O.; Nemes, R. Ba-IV-Type Incommensurate Crystal Structure in Group-V Metals. *Phys. Rev. Lett.* **2000**, *85*, 4896–4899.
- Schlickum, U.; Decker, R.; Klappenberger, F.; Zoppellaro, G.; Klyatskaya, S.; Auwärter, W.; Nepl, S.; Kern, K.; Brune, H.; Ruben, M.; *et al.* Chiral Kagomé Lattice from Simple Ditopic Molecular Bricks. *J. Am. Chem. Soc.* **2008**, *130*, 11778–11782.
- Tahara, K.; Furukawa, S.; Uji-i, H.; Uchino, T.; Ichikawa, T.; Zhang, J.; Mamdouh, W.; Sonoda, M.; Schryver, F. C. De; Feyter, S. De; *et al.* Two-Dimensional Porous Molecular Networks of Dehydrobenzo[12]annulene Derivatives via Alkyl Chain Interdigitation. *J. Am. Chem. Soc.* **2006**, *128*, 16613–1661325.
- Chen, B.; Zeng, X.; Baumeister, U.; Ungar, G.; Tschierske, C. Liquid Crystalline Networks Composed of Pentagonal, Square, and Triangular Cylinders. *Science* **2005**, *307*, 96–99.
- Takano, A.; Kawashima, W.; Noro, A.; Isono, Y.; Tanaka, N.; Dotera, T.; Matsushita, Y. A Mesoscopic Archimedean Tiling Having a New Complexity in an ABC Star Polymer. *J. Polym. Sci., Part B: Polym. Phys.* **2005**, *43*, 2427–2432.
- Talpin, D. V.; Shevchenko, E. V.; Bodnarchuk, M. I.; Ye, X.; Chen, J.; Murray, C. B. Quasicrystalline Order in Self-Assembled Binary Nanoparticle Superlattices. *Nature* **2009**, *461*, 964–967.
- Mikhael, J.; Roth, J.; Helden, L.; Bechinger, C. Archimedean-Like Tiling on Decagonal Quasicrystalline Surfaces. *Nature* **2008**, *454*, 501–504.
- Chen, Q.; Bae, S. C.; Granick, S. Directed Self-Assembly of a Colloidal Kagome Lattice. *Nature* **2011**, *469*, 381–384.
- Ithurria, S.; Tessier, M. D.; Mahler, B.; Lobo, R. P. S. M.; Dubertret, B.; Eros, A. L. Colloidal Nanoplatelets with Two-Dimensional Electronic Structure. *Nat. Mater.* **2011**, *10*, 936–941.
- Kavan, L.; Yum, J.-H.; Grätzel, M. Graphene Nanoplatelets Outperforming Platinum as the Electrocatalyst in Co-Bipyridine-Mediated Dye-Sensitized Solar Cells. *Nano Lett.* **2011**, *11*, 5501–5506.
- Lu, L.; Kobayashi, A.; Tawa, K.; Ozaki, Y. Silver Nanoplates with Special Shapes: Controlled Synthesis and Their Surface Plasmon Resonance and Surface-Enhanced Raman Scattering Properties. *Chem. Mater.* **2006**, *18*, 4894–4901.
- van Anders, G.; Ahmed, N.; Smith, R. Entropically Patchy Particles: Engineering Valence through Shape Entropy. *ACS Nano* **2014**, *8*, 931–940.
- Ye, X.; Chen, J.; Engel, M.; Millan, J. A.; Li, W.; Qi, L.; Xing, G.; Collins, J. E.; Kagan, C. R.; Li, J.; Glotzer, S. G.; *et al.* Competition of Shape and Interaction Patchiness for Self-Assembling Nanoplates. *Nat. Chem.* **2013**, *5*, 466–73.
- Smith, B. D.; Fichthorn, K. A.; Kirby, D. J.; Quimby, L. M.; Triplett, D. A.; González, P.; Hernández, D.; Keating, C. D. Asymmetric van der Waals Forces Drive Orientation of Compositionally Anisotropic Nanocylinders within Smectic Arrays: Experiment and Simulation. *ACS Nano* **2013** in press.
- Ando, T.; Takayanagi, K.; Kobayashi, K.; Chen, Z.; Lin, Y.-M.; Rooks, M. J.; Avouris, P. Graphene Nano-Ribbon Electronics. *Phys. E (Amsterdam, Neth.)* **2007**, *40*, 228–232.
- Chao, C.; Ren, Z.; Yin, S.; Gong, S.; Yang, X.; Xu, G.; Li, X.; Shen, G.; Han, G. Hydrothermal Synthesis of Ferroelectric PbTiO<sub>3</sub> Nanoparticles with Dominant {001} Facets by Titanate Nanostructure. *CrystEngComm* **2013**, *15*, 8036.
- Kim, Y.; Han, H.; Kim, Y.; Lee, W.; Alexe, M.; Baik, S.; Kim, J. K. Ultrahigh Density Array of Epitaxial Ferroelectric Nanoislands on Conducting Substrates. *Nano Lett.* **2010**, *10*, 2141–2146.
- Sau, T. K.; Murphy, C. J. Self-Assembly Patterns Formed upon Solvent Evaporation of Aqueous Cetyltrimethylammonium Bromide-Coated Gold Nanoparticles of Various Shapes. *Langmuir* **2005**, *21*, 2923–2929.
- Lee, J. A.; Meng, L.; Norris, D. J.; Scriven, L. E.; Tsapatsis, M. Colloidal Crystal Layers of Hexagonal Nanoplates by Convective Assembly. *Langmuir* **2006**, *22*, 5217–5219.
- Park, K. H.; Jang, K.; Son, S. U. Synthesis, Optical Properties, and Self-Assembly of Ultrathin Hexagonal In<sub>2</sub>S<sub>3</sub> Nanoplates. *Angew. Chem., Int. Ed.* **2006**, *45*, 4608–4612.
- Li, X.; Shen, H.; Niu, J.; Li, S.; Zhang, Y.; Wang, H.; Li, L. S. Columnar Self-Assembly of Cu<sub>2</sub>S Hexagonal Nanoplates Induced by Tin(IV)-X Complex as Inorganic Surface Ligand. *J. Am. Chem. Soc.* **2010**, *132*, 12778–12779.
- Ye, X.; Collins, J. E.; Kang, Y.; Chen, J.; Chen, D. T. N.; Yodh, A. G.; Murray, C. B. Morphologically Controlled Synthesis of Colloidal Upconversion Nanophosphors and Their Shape-Directed Self-Assembly. *Proc. Natl. Acad. Sci. U.S.A.* **2010**, *107*, 22430–22435.
- Shen, H.; Wang, H.; Yuan, H.; Ma, L.; Li, L. S. Size-, Shape-, and Assembly-Controlled Synthesis of Cu<sub>2</sub>-xSe Nanocrystals via a Non-Injection Phosphine-Free Colloidal Method. *CrystEngComm* **2012**, *14*, 555.
- Sun, Y.; Xia, Y. Shape-Controlled Synthesis of Gold and Silver Nanoparticles. *Science* **2002**, *298*, 2176–2179.
- Chen, Y.; He, X.; Zhao, X.; Yuan, Q.; Gu, X. Preparation, Characterization, and Growth Mechanism of a Novel Aligned Nanosquare Anatase in Large Quantities in the Presence of TMAOH. *J. Colloid Interface Sci.* **2007**, *310*, 171–177.
- Paik, T.; Ko, D.-K.; Gordon, T. R.; Doan-Nguyen, V.; Murray, C. B. Studies of Liquid Crystalline Self-Assembly of GdF<sub>3</sub> Nanoplates by in-Plane, out-of-Plane SAXS. *ACS Nano* **2011**, *5*, 8322–8330.
- Zhang, Y.-W.; Sun, X.; Si, R.; You, L.-P.; Yan, C.-H. Single-Crystalline and Monodisperse LaF<sub>3</sub> Triangular Nanoplates from a Single-Source Precursor. *J. Am. Chem. Soc.* **2005**, *127*, 3260–3261.
- Whitelam, S.; Tamblin, I.; Beton, P. H.; Garrahan, J. P. Random and Ordered Phases of Off-Lattice Rhombus Tiles. *Phys. Rev. Lett.* **2012**, *108*, 035702.
- Antlanger, M.; Doppelbauer, G.; Kahl, G. On the Stability of Archimedean Tilings Formed by Patchy Particles. *J. Phys.: Condens. Matter* **2011**, *23*, 404206.
- Pawar, A.; Kretschmar, I. Fabrication, Assembly, and Application of Patchy Particles. *Macromol. Rapid Commun.* **2010**, *31*, 150–168.

36. Iacovella, C. R.; Glotzer, S. C. Complex Crystal Structures Formed by the Self-Assembly of Ditettered Nanospheres. *Nano Lett.* **2009**, *9*, 1206–1211.
37. Sacanna, S.; Irvine, W. T. M.; Chaikin, P. M.; Pine, D. J. Lock and Key Colloids. *Nature* **2010**, *464*, 575–578.
38. Haji-Akbari, A.; Engel, M.; Keys, A. S.; Zheng, X.; Petschek, R. G.; Palfy-Muhoray, P.; Glotzer, S. C. Disordered, Quasi-crystalline and Crystalline Phases of Densely Packed Tetrahedra. *Nature* **2009**, *462*, 773–777.
39. Damasceno, P. F.; Engel, M.; Glotzer, S. C. Predictive Self-Assembly of Polyhedra into Complex Structures. *Science* **2012**, *337*, 453–457.
40. van Anders, G.; Ahmed, N. K.; Klotsa, D.; Engel, M.; Glotzer, S. C. Unified Theoretical Framework for Shape Entropy in Colloids. *arXiv:1309.1187*, **2013**.
41. Schapotschnikow, P.; Pool, R.; Vlugt, T. J. H. Molecular Simulations of Interacting Nanocrystals. *Nano Lett.* **2008**, *8*, 2930–2934.
42. de Vries, R. Depletion-Induced Instability in Protein-DNA Mixtures: Influence of Protein Charge and Size. *J. Chem. Phys.* **2006**, *125*, 014905.
43. Kaushik, A. P.; Clancy, P. Explicit All-Atom Modeling of Realistically Sized Ligand-Capped Nanocrystals. *J. Chem. Phys.* **2012**, *136*, 114702.
44. Ye, X.; Millan, J. A.; Engel, M.; Chen, J.; Diroll, B. T.; Glotzer, S. C.; Murray, C. B. Shape Alloys of Nanorods and Nanospheres from Self-Assembly. *Nano Lett.* **2013**, *13*, 4980–4988.
45. Damasceno, P. F.; Engel, M.; Glotzer, S. C. Crystalline Assemblies and Densest Packings of a Family of Truncated Tetrahedra and the Role of Directional Entropic Forces. *ACS Nano* **2012**, *6*, 609–614.
46. Young, K. L.; Personick, M. L.; Engel, M.; Damasceno, P. F.; Barnaby, S. N.; Bleher, R.; Li, T.; Glotzer, S. C.; Lee, B.; Mirkin, C. A. A Directional Entropic Force Approach to Assemble Anisotropic Nanoparticles into Superlattices. *Angew. Chem., Int. Ed.* **2013**, *52*, 13980–13984.
47. Wojciechowski, K. W.; Frenkel, D. Tetratic Phase in the Planar Hard Square System. *Comp. Met. Sci. Technol.* **2004**, *10*, 235–255.
48. Zhao, K.; Bruinsma, R.; Mason, T. G. Entropic Crystal-Crystal Transitions of Brownian Squares. *Proc. Natl. Acad. Sci. U.S.A.* **2011**, *108*, 2684–2687.
49. Zhao, K.; Bruinsma, R.; Mason, T. G. Local Chiral Symmetry Breaking in Triatic Liquid Crystals. *Nat. Commun.* **2012**, *3*, 801.
50. Duparcmeur, Y. L.; Gervois, A.; Troadec, J. P. Dense Periodic Packings of Regular Polygons. *J. Phys. I* **1995**, *5*, 1539–1550.
51. Dijkstra, M.; van Roij, R.; Evans, R. Phase Diagram of Highly Asymmetric Binary Hard-Sphere Mixtures. *Phys. Rev. E* **1999**, *59*, 5744–5771.
52. Demaine, E. D.; Demaine, M. L. Jigsaw Puzzles, Edge Matching, and Polyomino Packing: Connections and Complexity. *Graphs Comb.* **2007**, *23*, 195–208.
53. Fjærestad, J. O. The 3-Edge-Colouring Problem on the 4–8 and 3–12 Lattices. *J. Stat. Mech. Theory Exp.* **2010**, *2010*, P01004.
54. Chu, H.-C.; Kuo, C.-H.; Huang, M. H. Thermal Aqueous Solution Approach for the Synthesis of Triangular and Hexagonal Gold Nanoplates with Three Different Size Ranges. *Inorg. Chem.* **2006**, *45*, 808–813.
55. An, J.; Tang, B.; Ning, X.; Zhou, J.; Zhao, B.; Xu, W.; Corredor, C.; Lombardi, J. R. Photoinduced Shape Evolution: From Triangular to Hexagonal Silver Nanoplates. *J. Phys. Chem. C* **2007**, *111*, 18055–18059.
56. Xiong, Y.; McLellan, J. M.; Chen, J.; Yin, Y.; Li, Z.-Y.; Xia, Y. Kinetically Controlled Synthesis of Triangular and Hexagonal Nanoplates of Palladium and Their SPR/SERS Properties. *J. Am. Chem. Soc.* **2005**, *127*, 17118–171127.
57. Li, M.; Xu, L.; Sun, C.; Ju, Z.; Qian, Y. Thermal-Induced Shape Evolution from Uniform Triangular to Hexagonal r-BN Nanoplates. *J. Mater. Chem.* **2009**, *19*, 8086.
58. Guo, H.; Chen, Y.; Ping, H.; Wang, L.; Peng, D.-L. One-Pot Synthesis of Hexagonal and Triangular Nickel–Copper Alloy Nanoplates and Their Magnetic and Catalytic Properties. *J. Mater. Chem.* **2012**, *22*, 8336.
59. Zhou, B.; Ji, Y.; Yang, Y.-F.; Li, X.-H.; Zhu, J.-J. Rapid Microwave-Assisted Synthesis of Single-Crystalline Sb<sub>2</sub>Te<sub>3</sub> Hexagonal Nanoplates. *Cryst. Growth Des.* **2008**, *8*, 4394–4397.
60. Xu, F.; Yuan, Z.-Y.; Du, G.-H.; Halasa, M.; Su, B.-L. High-Yield Synthesis of Single-Crystalline ZnO Hexagonal Nanoplates and Accounts of Their Optical and Photocatalytic Properties. *Appl. Phys. A: Mater. Sci. Process.* **2006**, *86*, 181–185.
61. Wang, H.; Casalongue, H. S.; Liang, Y.; Dai, H. Ni(OH)<sub>2</sub> Nanoplates Grown on Graphene as Advanced Electrochemical Pseudocapacitor Materials. *J. Am. Chem. Soc.* **2010**, *132*, 7472–7477.
62. Chuan, Z.; Zhu, Y. Synthesis of Square Bi<sub>2</sub>WO<sub>6</sub> Nanoplates as High-Activity Visible-Light-Driven Photocatalysts. *Chem. Mater.* **2005**, *17*, 3537–3545.
63. Su, X.; Xiao, F.; Li, Y.; Jian, J.; Sun, Q.; Wang, J. Synthesis of Uniform WO<sub>3</sub> Square Nanoplates via an Organic Acid-Assisted Hydrothermal Process. *Mater. Lett.* **2010**, *64*, 1232–1234.
64. Cao, Y. C. Synthesis of Square Gadolinium-Oxide Nanoplates. *J. Am. Chem. Soc.* **2004**, *126*, 7456–7457.
65. Park, M.; Lee, N.; Choi, S. H.; An, K.; Yu, S.-H.; Kim, J. H.; Kwon, S.-H.; Kim, D.; Kim, H.; Baek, S. I.; *et al.* Large-Scale Synthesis of Ultrathin Manganese Oxide Nanoplates and Their Applications to T1MRI Contrast Agents. *Chem. Mater.* **2011**, *23*, 3318–3324.
66. Xi, G.; Ye, J. Synthesis of Bismuth Vanadate Nanoplates with Exposed {001} Facets and Enhanced Visible-Light Photocatalytic Properties. *Chem. Commun. (Cambridge)* **2010**, *46*, 1893–1895.
67. Paik, T.; Gordon, T. R.; Prantner, A. M.; Yun, H.; Murray, C. B. Designing Tripodal and Triangular Gadolinium Oxide Nanoplates and Self-Assembled Nanofibrils as Potential Multimodal Bioimaging Probes. *ACS Nano* **2013**, *7*, 2850–2859.
68. Kan, C.; Wang, C.; Li, H.; Qi, J.; Zhu, J.; Li, Z.; Shi, D. Gold Microplates with Well-Defined Shapes. *Small* **2010**, *6*, 1768–1775.
69. Zeng, Y.; Li, H.; Xiang, B.; Ma, H.; Qu, B.; Xia, M.; Wang, Y.; Zhang, Q.; Wang, Y. Synthesis and Characterization of Phase-Purity Cu<sub>9</sub>BiS<sub>6</sub> Nanoplates. *Mater. Lett.* **2010**, *64*, 1091–1094.
70. Nykpanchuk, D.; Maye, M. M.; van der Lelie, D.; Gang, O. DNA-Guided Crystallization of Colloidal Nanoparticles. *Nature* **2008**, *451*, 549–552.
71. Macfarlane, R. J.; Lee, B.; Jones, M. R.; Harris, N.; Schatz, G. C.; Mirkin, C. A. Nanoparticle Superlattice Engineering with DNA. *Science* **2011**, *334*, 204–208.
72. Gilbert, E. G.; Johnson, D. W.; Keerthi, S. S. A Fast Procedure for Computing the Distance Between Complex Objects in Three-Dimensional Space. *IEEE J. Robot. Autom.* **1988**, *4*, 193–203.